Journal of Magnetic Resonance **143,** 376–381 (2000)
doi:10.1006/jmre.1999.1999, available online at http://www.idealibrary.com on IDEAL®

NMR Characterization of the Pore Structure and Anisotropic Self-Diffusion in Salt Water Ice

Marion I. Menzel, Song-I Han, Siegfried Stapf, and Bernhard Blümich

Institut für Technische Chemie und Makromolekulare Chemie and Magnetic Resonance Center MARC, RWTH Aachen, D-52074 Aachen, Germany

Received August 26, 1999; revised December 1, 1999

NMR imaging and one- and two-dimensional self-diffusion propagator measurements of the liquid phase in salt water ice are presented. The properties of the network of brine-filled pores are found to depend on the growth conditions of the ice. Two types of samples are compared: (a) shock-frozen ice produced in the probe *in situ* and (b) ice grown over several hours under controlled conditions. By shock-freezing, an ice structure could be produced which featured streak-like porous channels of diameters of up to 300 μm allowing almost unrestricted self-diffusion along one preferential axis but reduced diffusivities in the remaining directions. In ice grown under controlled conditions, the pore sizes are near the resolution limit of the imaging experiment of typically 50 μm. For this type of samples, strongly non-Gaussian self-diffusion propagators are obtained, indicating restricted self-diffusion on rms scales of 30 μm. Common to all samples was the observation of highly anisotropic self-diffusion. One- and two-dimensional propagators are compared in order to estimate the degree of anisotropy and the size of the restrictions.

Key Words: **sea water; ice; porous media; restricted diffusion; propagator.**

INTRODUCTION

Sea ice covers up to 5% of the Earth's surface area, and understanding its exceptional importance for the regulation of the earth's climate is intimately linked to a detailed knowledge of its thermal, optical, and mechanical properties. At the same time, sea ice plays a dominant role in the transport of contaminants throughout the polar oceans and their exchange with sea water. The rich reserves of crude oil found in the Arctic shelf and coastal regions constitute the quantitatively largest portion of contaminants. Anthropogenous sources such as oil exploitation and, more recently, the opening of the Northern Sea Route for commercial transport represent a severe threat to the marine ecosystem and already account for a total contaminant volume exceeding the natural influx by far (*1*). The problem of oil in sea ice has been addressed in a number of review articles (*2–5*).

The ingress of oil into ice is mainly determined by the structure of the porous network which is generated by a process of recrystallization and phase separation into pockets of concentrated brine surrounded by freshwater ice (*6*). This network also serves as an environment for wintering algae and higher organisms (*7*) which are vulnerable to oil and other contaminants such as heavy metals. Understanding the properties of the pore space thus is a prerequisite for modeling the transport behavior of these contaminants.

In sea water, freezing of the aqueous phase begins at approximately −2°C while a separation between freshwater ice and brine occurs as the temperature decreases, leading to an increasing salinity in brine-filled pores (*6*). Because sodium chloride constitutes the largest fraction of the salts present in sea water, a 3% w/w aqueous solution of sodium chloride represents a reasonable approximation of the natural conditions. In this system, the concentrated brine eventually freezes at the temperature of the eutecticum, −21.2°C at 23% w/w salt concentration. In the intermediate temperature range, the properties of the porous network depend strongly not only on the temperature but also on the growth and storage history of the ice. To our knowledge, NMR images of the brine distribution in salt water ice were reported only twice in the literature (*8, 9*). In Ref. (*8*), columnar ice was prepared from an aqueous solution of a salt mixture very similar to the salt distribution in sea water, and an in-plane resolution of 500 μm was achieved. Channels with diameters of up to 2 mm were found. More recently, the distribution of crude oil contaminating sea ice was shown by images obtained with a clinical imaging system (*10*).

In the present work, the dependence of the pore structure on growth conditions is investigated by comparing ice samples prepared from identical 3% NaCl solutions but grown under different conditions. Conventional NMR imaging is employed to reveal pore structures on scales down to 50–100 μm. Below this resolution limit, complementary information is obtained by pulsed field gradient techniques which probe the dispersion properties of the liquid phase. From these measurements, the propagator, or probability density of displacements, averaged over a slice of the sample, is obtained (*11*). Propagators determined by applying pulsed gradients in different directions are one possibility for comparing the dispersion processes along different axes in the sample (*12–14*). Results for the direction parallel and perpendicular to the growth axis are discussed. By stepping gradients along two orthogonal directions simultaneously but independently from each other, two-dimensional

1090-7807/00 $35.00

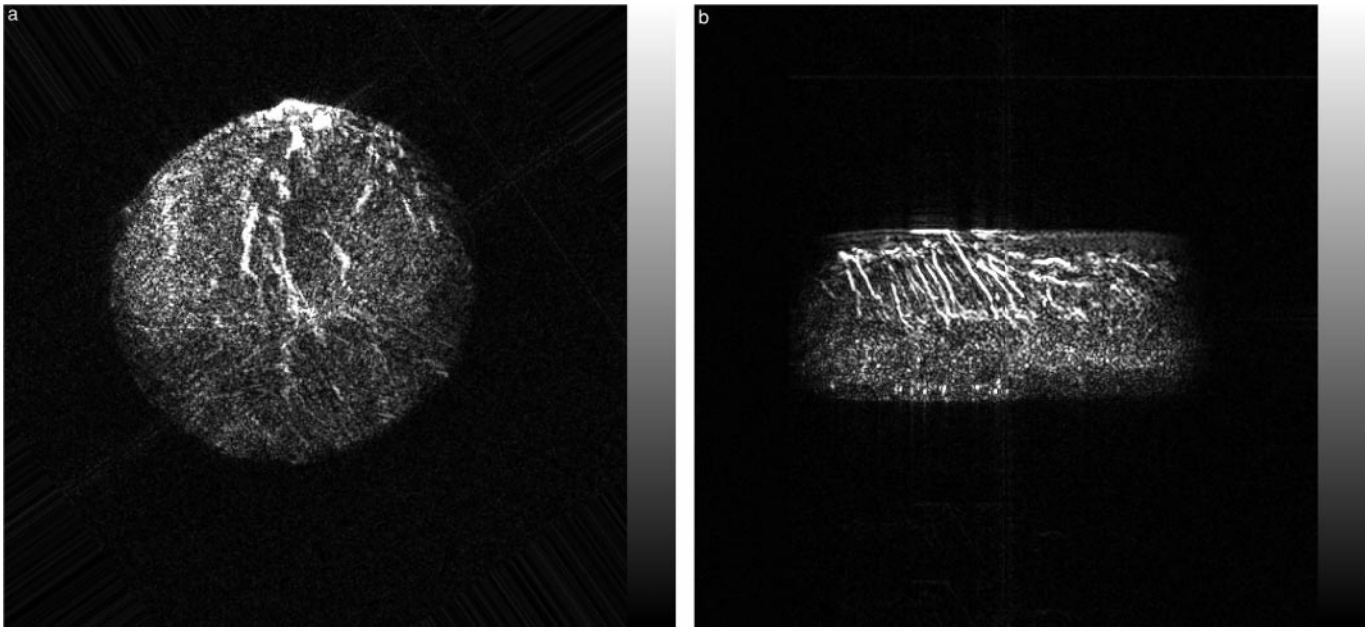

FIG. 1. Spin-density image of a sample of type Ice A. Acquisition parameters: slice thickness: 2.7 mm, echo time: 7 ms, number of accumulations: 32. Signal intensity corresponds to brine concentration in the selected slice. (a) Cross-sectional image. The sample diameter is 15 mm; the resolution is 100 × 100 μm. (b) Longitudinal section; resolution 230 × 230 μm.

propagators can be obtained, revealing possible correlations between displacements along different axes (*15–17*). Moreover, the shapes of the propagators contain information about the nature and the size of geometrical restrictions (*18–20*). A tentative interpretation is given which helps to conduct future investigations of single- and multiphase fluid transport in artificial salt water ice and sea ice.

EXPERIMENTAL

The measurements were performed on a horizontal 7-T, 20-cm bore magnet equipped with a Bruker DMX-300 spectrometer. Sample tubes of 15 mm ID and 100 mm length were placed horizontally in a 25-mm resonator and held at constant temperature (−15°C) in a stream of nitrogen gas along the long axis of the sample. For the first series of experiments, the tubes were filled with 3% w/w aqueous NaCl solution and cooled *in situ* from room temperature to ca. −40°C over a time of about 1 h. These shock-frozen samples (Ice A) were then heated to the desired temperature and measured shortly afterward. The second sample type was prepared in a cylindrical container of 15 mm ID and 40 mm height and was placed in a constant temperature gradient where the upper end was kept at −20°C and the lower end at −2°C. The ice was grown by this method over a period of 6 h and subsequently stored at −80°C to prevent recrystallization until the beginning of the experiment. For this second sample type (Ice B), the growth axis of the ice crystals, equivalent to the direction of both gravity and temperature gradient, was oriented along the axis of the cylinder and corresponded to the direction z of the B_0 field of the spectrometer. For comparison, a third set of ice samples was prepared in the freezing compartment of a refrigerator at −15°C and stored at this temperature for days to weeks before the measurements were performed (Ice C). All experiments were repeated on at least two to three different samples and the behavior was found to match qualitatively for a given sample type, proving the reproducibility of the preparation procedure.

Two-dimensional images were obtained using a conventional spin-echo sequence with echo times of 7 ms and slice thicknesses between 1.0 and 2.7 mm. The one-dimensional propagators were measured using a stimulated-echo sequence (*21*) with pulsed field gradient lengths δ of 1.5 or 2.5 ms and an encoding time $\Delta = 2.0$ s between the centers of the gradient pulses. Measurements were performed with the gradients subsequently oriented in three orthogonal directions x, y, and z. Two-dimensional propagators were obtained by simultaneous application of gradient pulses along axes parallel and perpendicular to the crystal growth axis. The gradients were varied between $-q_{\max}$ and $q_{\max}$ in 129 steps (1D) and 33 × 33 steps (2D), respectively, where $q_{\max}$ represents the maximum applied gradient strength.

RESULTS AND DISCUSSION

Imaging

In Fig. 1 we present proton spin-density images of shock-frozen 3% w/w NaCl aqueous solution (Ice A). The images

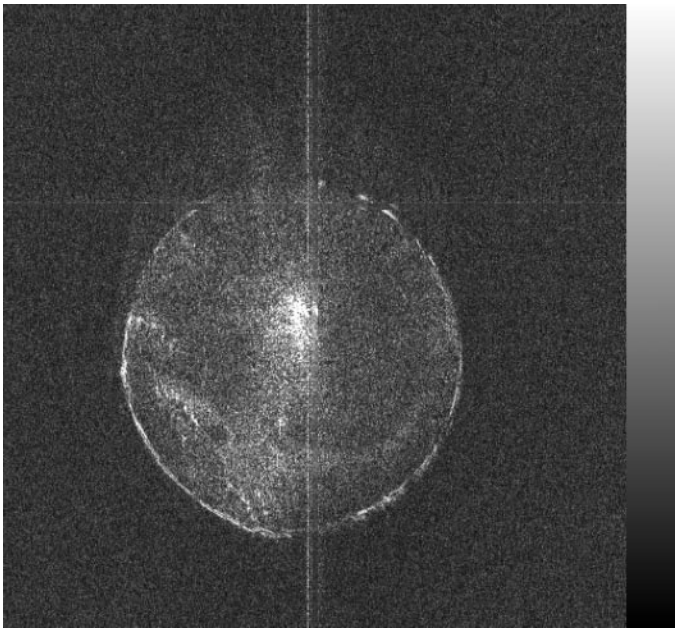

FIG. 2. Cross-sectional spin-density image of a sample of type Ice B. Acquisition parameters: slice thickness: 1.46 mm, echo time: 7 ms, number of accumulations: 8. Signal intensity corresponds to brine concentration in the selected slice. The sample diameter is 15 mm; the resolution is 25 × 50 μm.

were obtained with 32 accumulations at a slice thickness of 2.7 mm each. In Fig. 1a, a cross section in the x, y plane is shown, while Fig. 1b represents the central slice of the x, z plane. The resolution is 256 × 256 points corresponding to a pixel size of 100 μm for the x/y image and 230 μm for the x/z image, respectively.

Due to the extremely short T_2 of protons in water ice, the signal corresponds entirely to the aqueous NaCl solution in the liquid state. At the temperature of −15°C, where the image was taken, the total signal amplitude has decreased to roughly 20% of its value above the melting point, in good agreement with values found in the literature for sea ice (*6, 22, 23*).

The images in Figs. 1a and 1b clearly show a connected network of pores of up to 300 μm diameter and 8 mm in length. The sample was cooled by nitrogen gas flow from the front end (left in Fig. 1b). The dominating structural features in the spin-density images, however, are oriented parallel to the gravity axis. By acquiring a series of images during the cooling process it became obvious that freezing occurred first at the top of the sample. This growth process is reflected by the distribution of the majority of large channels.

In Fig. 2, the spin-density distribution is shown for an x/y slice in a sample grown in a controlled temperature gradient as described above (Ice B). The image was obtained using eight accumulations and a slice thickness of 1.46 mm. The resolution is 1024 × 512 points, corresponding to 25 μm in the x (read) direction and 50 μm in y (phase) direction. Contrary to the sample presented in Fig. 1, no large features are observed apart from an increased signal intensity in the core and at the edge of the ice cylinder, the latter probably being a consequence of melting during the process of sample change into the NMR glass cylinder and subsequent recrystallization. An intermediate behavior was found for images taken under similar conditions of samples of type Ice C, with weakly pronounced pore structures of up to 200 μm diameter and 2 mm in length (data not shown).

Self-diffusion Measurements

While large pores can be imaged directly by NMR, small structures below the resolution limit are also expected to exist in ice (*24*). They can be investigated in an indirect way by allowing the liquid water to probe the topology of the pore space by its self-diffusion. Monitoring the signal intensity following a PGSTE pulse sequence (*21*) as a function of the wave vector, $\mathbf{q}$, where $\mathbf{q} = (2\pi)^{-1}\gamma\delta\mathbf{G}$ and δ and $\mathbf{G}$ are duration and strength of the identical gradient pulses, respectively, directly gives the propagator (*11*), $P_\Delta(\mathbf{R})$, by subsequent Fourier transformation with respect to $\mathbf{q}$:

$$S_\Delta(\mathbf{q}) = \int P_\Delta(\mathbf{R})\, \exp\{i2\pi\mathbf{q}\cdot\mathbf{R}(\Delta)\}d\mathbf{R}, \qquad [1]$$

where $P_\Delta(\mathbf{R}) = P(\mathbf{r}_0)P(\mathbf{r}, \Delta; \mathbf{r}_0)d\mathbf{r}_0$. $P(\mathbf{r}_0)$ is the probability density for starting positions, while $P(\mathbf{r}, \Delta; \mathbf{r}_0)$ is the conditional probability for displacements from $\mathbf{r}_0$ to $\mathbf{r}$ in time Δ. The propagator thus averages over all starting positions of the particles. Because the dispersion of fluid molecules corresponds to a mapping of the porous network, the method has been described as q-space imaging (*19*), providing statistical rather than direct topological information.

P_Δ is given by a Gaussian in the case of unrestricted self-diffusion. This is always the case when the rms displacements are much smaller than the pore dimensions, corresponding to the limit of short times:

$$\lim_{\Delta\to 0} P_\Delta(X, Y, Z) = \lim_{\Delta\to 0} \prod_{j=1,3} P_\Delta(\xi_j)$$

$$= \lim_{\Delta\to 0} (4\pi\Delta D_0)^{-3/2} \prod_{j=1,3} \exp\left[-\frac{\xi_j^2}{4D_0\Delta}\right], \qquad [2]$$

where D_0 is the bulk self-diffusion coefficient, and $\xi_j = X, Y, Z$ for $j = 1, 2, 3$. All possible projections of $P_\Delta(X, Y, Z)$ are identical Gaussians. For longer times, when the particle has a nonnegligible probability to "see" a wall, the shape of the propagator deviates from a Gaussian (*20*). Moreover, macroscopic anisotropies in the pore space lead to a diffusivity which depends on the direction of the applied gradient, so that in general $D_x \neq D_y \neq D_z$.

In Fig. 3, the shapes of the one-dimensional propagators are

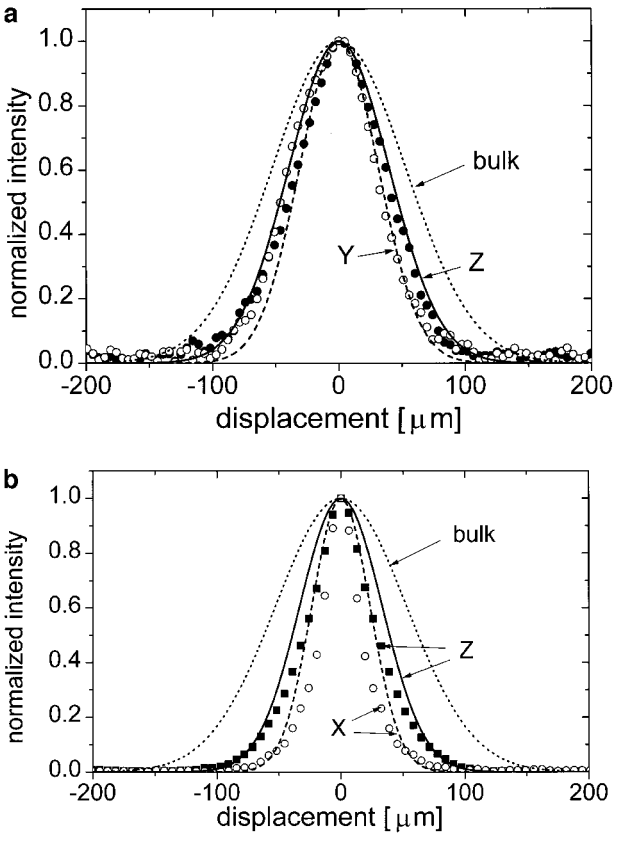

FIG. 3. Average propagators, P_Δ, for self-diffusion in ice at a diffusion time of $\Delta = 2.0$ s. Solid and dashed lines represent fits of a Gaussian to the experimental data; the dotted line corresponds to the measurements performed on a saturated NaCl solution at the same temperature. Directions of displacements as indicated. (a) Ice A; (b) Ice B.

compared for both types of ice samples. The measurements were performed immediately following the acquisition of the images shown in Figs. 1 and 2, so that the ice morphology is directly comparable.

Propagators in two directions for Ice A are shown in Fig. 3a. Solid lines represent fits to the experimental data corresponding to a Gaussian propagator of identical second moment. The deviation of the general shape of the measured propagators from a Gaussian is minor. For comparison, the propagator of a saturated NaCl solution at the same temperature is given by the dotted line; this experiment was performed in a tube containing glass wool to prevent convective motions. The spreading of particles in the pore space clearly is smaller than for bulk diffusion, indicating the influence of geometrical restrictions.

This difference in the spread is more pronounced in the case of Ice B (Fig. 3b). A strong anisotropy is observed between diffusion parallel (Z) and perpendicular (X, Y) to the growth axis. Moreover, the deviation of the propagator shape from a Gaussian becomes obvious from a comparison with the fitted curves. To demonstrate the anisotropy of the self-diffusion process, a two-dimensional propagator was obtained under the same conditions as the measurements presented above (*16*). In Fig. 4, the ellipsoidal shape of the displacement probability density is clearly seen. A correlation analysis performed on this experiment (see, for example, (*16*)) renders a small but significant positive correlation coefficient $\rho_{X^2,Z^2} = 0.08 \pm 0.03$, indicating that particles with large $\langle Z^2 \rangle$ tend to possess large $\langle X^2 \rangle$ as well.

Unless very long times are regarded where the molecules sample a space containing a representative distribution of all pore sizes, the effective self-diffusion coefficients will remain a function of time, Δ. The dispersion of fluid particles is then best described by the second moment of the displacements,

$$\langle \xi_j^2(\Delta) \rangle = \int P_\Delta(\xi_j) \xi_j^2 d\xi_j. \qquad [3]$$

The effective self-diffusion coefficient is defined by the time-derivative of the second moment, for example,

$$D_x = \frac{d\langle (X - \langle X \rangle)^2 \rangle}{d\Delta}. \qquad [4]$$

Rather than determining it directly from an integral over the propagator, the effective self-diffusion coefficient can also be obtained from the low-q behavior of the signal function $S(q)$ in the narrow gradient ($\delta \ll \Delta$) approximation (*25*):

$$D(\Delta) \approx -(4\pi^2\Delta)^{-1} \lim_{q \to 0} \frac{\partial \ln|E_\Delta(q)|}{\partial q^2}, \qquad [5]$$

where $E_\Delta(q) = S_\Delta(q)/S_\Delta(0)$ is the normalized echo intensity.

In Fig. 5, the diffusional decay curves are compared for the propagators presented in Fig. 3. In a semi-logarithmic plot of

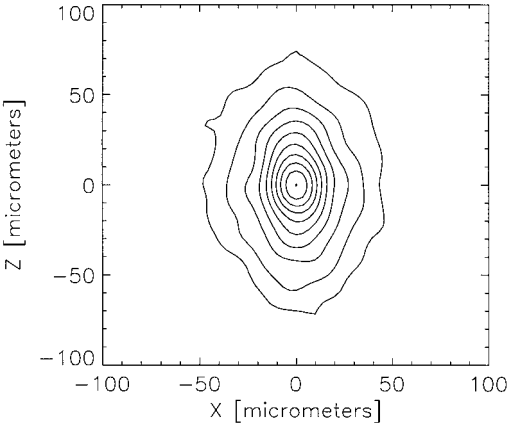

FIG. 4. Two-dimensional propagator, $P_\Delta(X, Z)$, for self-diffusion in Ice B. Contour lines represent probability densities in 10% intervals with the maximum value being normalized to unity.

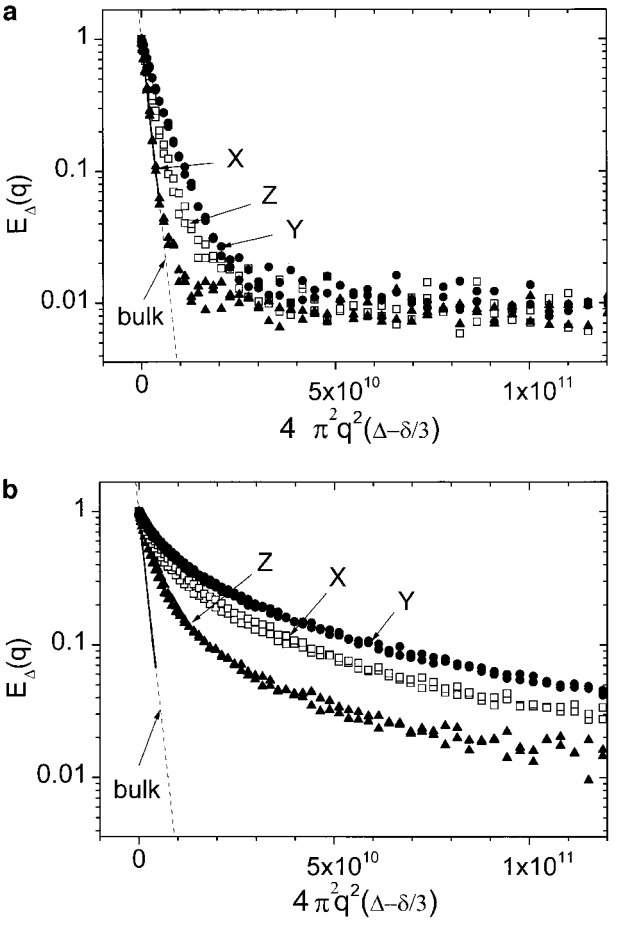

FIG. 5. Diffusional decay curves corresponding to the propagators of Fig. 3. The solid lines represent experimental data for a saturated NaCl solution, which are extrapolated by the dashed line. (a) Ice A; (b) Ice B.

$E_\Delta(q)$ as a function of $4\pi^2q^2(\Delta - \delta/3)$, a straight line represents undisturbed self-diffusion. This is approximately observed in the case of Ice A (Fig. 5a), where the decay is exponential over more than one order of magnitude. However, as is indicated by the decay curve obtained for the liquid NaCl solution (corresponding to $D_0 = 7.0 \times 10^{-10}$ m^2 s^{-1}), self-diffusion is slowed down compared to the bulk liquid, the measured diffusion coefficients being $D_x = 0.90D_0$, $D_y = 0.35D_0$, and $D_z = 0.57D_0$, respectively, while the predominant direction of ice growth is along the x axis.

For Ice B, the nonexponential nature of the diffusional decay becomes much more pronounced (Fig. 5b), a result which is expected when a significant number of pores is found with sizes below the resolution limit of the imaging experiments. On the other hand, if the largest pores would have diameters much smaller than the rms displacement, an averaged but reduced self-diffusion coefficient and a Gaussian propagator are expected. From the values fitted to the experimental data ($D_x = 0.23D_0$, $D_y = 0.17D_0$, and $D_z = 0.40D_0$, with the growth direction now being parallel to the z axis), rms displacements between 20 and 35 μm are obtained. The presence of pores of this size in Ice B is therefore necessitated by the shape of the diffusional decay curve. Similar results, but with a less pronounced flattening of the decay curve, were also obtained for samples of Ice C.

The observations made for artificial ice can be compared to the situation in naturally grown Antarctic sea ice where diffusion was found to be anisotropic and restricted on similar length scales (*26*). Although indications for an enhanced diffusion process, which was also discussed in (*26*), were found in some experiments on larger pore samples of Ice A, possible contributions of a suggested convection mechanism must be investigated in more detail.

CONCLUSIONS

In this work we have attempted to combine methods of k-space and q-space imaging to investigate the structure of the pore network in salt water ice. Conventional imaging is sufficient to analyze orientation and size of large pores which are produced by either fast freezing processes or by continuous melting and recrystallization as observed in the Arctic and Antarctic environment. Small pores, however, have the effect to restrict diffusion, and their anisotropic growth pattern clearly shows up when diffusion propagators are obtained in different spatial directions. Restrictions and anisotropies in the diffusional behavior were found to be most obvious in samples of ice grown slowly under controlled conditions, but were observed in all samples under investigation. Describing the connectivity of the porous network is a first step to understanding how contaminants such as crude oil enter the pore space and affect life forms present in natural sea ice. To obtain a better match with the real situation, applications of the described methods to sea ice and to laboratory-grown ice with different concentrations of contaminants are currently being performed, and a more sophisticated data inversion shall obtain a measure for pore size distributions and pore space connectivities. In combination with mobile spectrometer equipment (*27*), applying k-space and q-space imaging bears the potential of providing a noninvasive tool for monitoring the seasonal changes of ice structure in polar environments.

ACKNOWLEDGMENTS

We are grateful to H. Schoof and I. Heschel for preparing the ice samples and to P. Blümler and K. Kupferschläger for their support in setting up the experiments. Helpful discussions with B. Pfleiderer, M. A. Lange, and U. Buschmann are gratefully acknowledged.

REFERENCES

1. "Arctic Pollution Issues: A State of the Arctic Environment Report," Arctic Monitoring and Assessment Programme (AMAP), Oslo (1997).
2. G. Futsaeter, G. Eidnes, G. Halmo, S. Johansen, H. P. Mannvik,

L. K. Sydnes, and U. Witte, Report on oil pollution, *in* "The State of the Arctic Environment," pp. 270–334, Arctic Centre, University of Lapland, Rovaniemi (1991).

3. J. R. Payne, G. D. McNabb, and J. R. Clayton, Oil weathering behaviour in Arctic environments, *in* "Proceedings of the Pro Mare Symposium on Polar Ecology" (E. Sakshaug, C. C. E. Hopkins, and N. A. Øritsland, Eds.), pp. 631–662, Trondheim (1991).
4. L. K. Sydnes, Oil, water, ice and light, *in* "Proceedings of the Pro Mare Symposium on Polar Ecology" (E. Sakshaug, C. C. E. Hopkins, and N. A. Øritsland, Eds.), pp. 609–618, Trondheim (1991).
5. "AMAP Assessment Report: Arctic Pollution Issues," Arctic Monitoring and Assessment Programme (AMAP), Oslo (1998).
6. W. F. Weeks and S. F. Ackley, CRREL Rep. 82-1, Cold. Reg. Res. Eng. Lab., Hanover, NH (1982).
7. J. Weissberger, The environmental conditions in the brine channels of Antarctic sea-ice, *Ber. Polarforsch.* **111,** 1–159 (1992).
8. W. A. Edelstein and E. M. Schulson, *J. Glaciol.* **37,** 125 (1991).
9. P. Callaghan and C. Eccles, *Bull. Magn. Reson.* **18,** 62 (1996).
10. B. Pfleiderer, U. Buschmann, and M. A. Lange, private communication.
11. J. Kärger and W. Heink, *J. Magn. Reson.* **51,** 1 (1983).
12. M. H. G. Amin, S. J. Gibbs, R. J. Chorley, K. S. Richards, T. A. Carpenter, and L. D. Hall, *Proc. Roy. Soc. Lond. A* **453,** 489 (1997).
13. J. J. Tessier, K. J. Packer, J.-F. Thovert, and P. M. Adler, *AIChE J.* **43,** 1653 (1997).
14. U. Tallarek, D. van Dusschoten, H. Van As, E. Bayer, and G. Guiochon, *J. Phys. Chem. B* **102,** 3486 (1998).
15. K. J. Packer, S. Stapf, J. J. Tessier, and R. A. Damion, *Magn. Reson. Imaging* **16,** 463 (1998).
16. S. Stapf, K. J. Packer, R. G. Graham, J.-F. Thovert, and P. M. Adler, *Phys. Rev. E* **58,** 6206 (1998).
17. V. Göbbels, "Zweidimensionale Magnetische Resonanz an porösen Medien," Dissertation, RWTH Aachen (1999).
18. P. T. Callaghan, D. MacGowan, K. J. Packer, and F. O. Zelaya, *Magn. Reson. Imaging* **9,** 663 (1991).
19. P. T. Callaghan, S. L. Codd, and J. D. Seymour, *Concepts Magn. Reson.* **11,** 181 (1999).
20. S. Stapf, K. J. Packer, and P. M. Adler, submitted for publication.
21. E. O. Stejskal, and J. E. Tanner, *J. Chem. Phys.* **42,** 288 (1965).
22. C. Richardson and E. E. Keller, *J. Glaciol.* **6,** 89 (1966).
23. G. Frankenstein and R. Garner, *J. Glaciol.* **6,** 943 (1967).
24. D. K. Perovich and A. J. Gow, *J. Geophys. Res.* **101,** 18327 (1996).
25. P. T. Callaghan and J. Stepišnik, *Adv. Magn. Opt. Reson.* **19,** 325 (1996).
26. P. T. Callaghan, C. D. Eccles, T. G. Haskell, P. J. Langhorne, and J. D. Seymour, *J. Magn. Reson.* **133,** 148 (1998).
27. B. Blümich, P. Blümler, G. Eidmann, A. Guthausen, R. Haken, U. Schmitz, K. Saito, and G. Zimmer, *Magn. Reson. Imaging* **16,** 479 (1998).